7-1-2023

Multiparametric immunoimaging maps inflammatory signatures in murine myocardial infarction models

Alexander Maier
Mount Sinai School of Medicine
Gyu Seong Heo
Washington University School of Medicine in St. Louis
Robert J Gropler
Washington University School of Medicine in St. Louis
Yongjian Liu
Washington University School of Medicine in St. Louis
et al.

JACC: BASIC TO TRANSLATIONAL SCIENCE VOL. 8, NO. 7, 2023

ORIGINAL RESEARCH - PRECLINICAL

Multiparametric Immunoimaging Maps Inflammatory Signatures in Murine Myocardial Infarction Models

Alexander Maier, MD,[a,b,c] Yohana C. Toner, BSc,[a,b,d] Jazz Munitz, BSc,[a,b] Nathaniel A.T. Sullivan, MS,[a,b] Ken Sakurai, PhD,[a,b] Anu E. Meerwaldt, MSc,[a,b,e] Eliane E.S. Brechbühl, MSc,[a,b] Geoffrey Prévot, PhD,[a,b] Yuri van Elsas, BSc,[a,b,d] Rianne J.F. Maas, MSc,[a,b,d] Anna Ranzenigo, PhD,[a,b] Georgios Soultanidis, PhD,[a,b] Mohammad Rashidian, PhD,[f,g] Carlos Pérez-Medina, PhD,[a,b,h] Gyu Seong Heo, PhD,[i] Robert J. Gropler, MD,[i] Yongjian Liu, PhD,[i] Thomas Reiner, PhD,[j] Matthias Nahrendorf, MD, PhD,[k] Filip K. Swirski, PhD,[l] Gustav J. Strijkers, PhD,[a,b,m] Abraham J.P. Teunissen, PhD,[a,b,l,n] Claudia Calcagno, MD, PhD,[a,b] Zahi A. Fayad, PhD,[a,b] Willem J.M. Mulder, PhD,[a,b,d,o] Mandy M.T. van Leent, MD, PhD[a,b,l]

VISUAL ABSTRACT

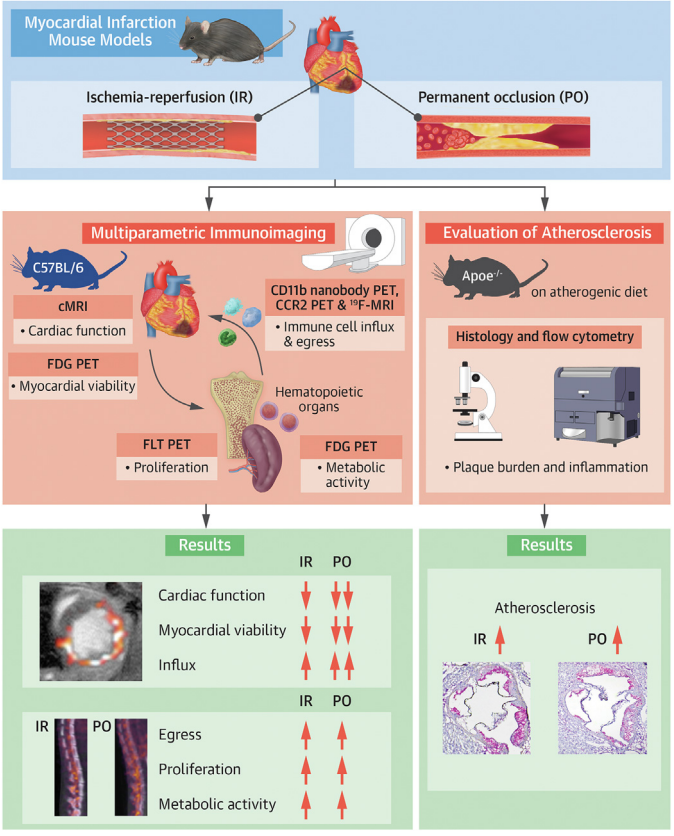

Maier A, et al. J Am Coll Cardiol Basic Trans Science. 2023;8(7):801-816.

HIGHLIGHTS

- **Preclinical PET and MR imaging methods can be used to characterize the immune response in the heart, bone marrow and spleen following myocardial infarction.**
- **Permanent coronary artery occlusion triggers the infiltration of more inflammatory cells into the myocardium as compared to the ischemia and reperfusion model.**
- **Bone marrow and spleen immune responses are similar in ischemia-reperfusion and permanent occlusion.**
- **Atherosclerosis accelerates in both types of myocardial infarction.**

ISSN 2452-302X https://doi.org/10.1016/j.jacbts.2022.12.014

JACC: BASIC TO TRANSLATIONAL SCIENCE VOL. 8, NO. 7, 2023
JULY 2023:801–816

ABBREVIATIONS AND ACRONYMS

CT = computed tomography

FDG = fluorodeoxyglucose

FLT = fluorothymidine

IR = ischemia-reperfusion

LAD = left anterior descending coronary artery

LGE = late gadolinium enhancement

MRI = magnetic resonance imaging

PET = positron emission tomography

PO = permanent occlusion

SUMMARY

In the past 2 decades, research on atherosclerotic cardiovascular disease has uncovered inflammation to be a key driver of the pathophysiological process. A pressing need therefore exists to quantitatively and longitudinally probe inflammation, in preclinical models and in cardiovascular disease patients, ideally using noninvasive methods and at multiple levels. Here, we developed and employed *in vivo* multiparametric imaging approaches to investigate the immune response following myocardial infarction. The myocardial infarction models encompassed either transient or permanent left anterior descending coronary artery occlusion in C57BL/6 and $Apoe^{-/-}$mice. We performed nanotracer-based fluorine magnetic resonance imaging and positron emission tomography (PET) imaging using a CD11b-specific nanobody and a C-C motif chemokine receptor 2-binding probe. We found that immune cell influx in the infarct was more pronounced in the permanent occlusion model. Further, using ^{18}F-fluorothymidine and ^{18}F-fluorodeoxyglucose PET, we detected increased hematopoietic activity after myocardial infarction, with no difference between the models. Finally, we observed persistent systemic inflammation and exacerbated atherosclerosis in $Apoe^{-/-}$ mice, regardless of which infarction model was used. Taken together, we showed the strengths and capabilities of multiparametric imaging in detecting inflammatory activity in cardiovascular disease, which augments the development of clinical readouts. (J Am Coll Cardiol Basic Trans Science 2023;8:801–816)

The immune reaction to acute myocardial infarction comprises a complex interplay between inflammation and repair. Either insufficient or overly active immune responses can be harmful, negatively affecting patient recovery and prognosis.[1,2] For example, inadequate activation of reparative programs can lead to infarct expansion, which increases the risk of subsequent heart failure,[3,4] whereas an exacerbated immune response can cause harm systemically. In the context of cardiovascular disease, excessive monocytosis after myocardial infarction accelerates atherosclerosis development.[5] A detailed understanding of these processes is therefore of substantial clinical importance.

Our view of the complex immune mechanisms that follow myocardial infarction is primarily built on research with a murine model of permanent coronary artery occlusion.[6] Although this model can enable important insights, it may not mimic the clinically more relevant cardiac ischemia and reperfusion scenario. Animal models of temporary coronary artery occlusion, however, do simulate blood flow restoration by percutaneous coronary intervention, the standard care for patients who experience a

From the [a]BioMedical Engineering and Imaging Institute, Icahn School of Medicine at Mount Sinai, New York, New York, USA; [b]Department of Diagnostic, Molecular, and Interventional Radiology, Icahn School of Medicine at Mount Sinai, New York, New York, USA; [c]Department of Cardiology and Angiology I, Heart Center of Freiburg University, Faculty of Medicine, University of Freiburg, Freiburg, Germany; [d]Department of Internal Medicine and Radboud Institute for Molecular Life Sciences, Radboud University Medical Center, Nijmegen, the Netherlands; [e]Biomedical Magnetic Resonance Imaging and Spectroscopy Group, Center for Image Sciences, University Medical Center Utrecht/Utrecht University, Utrecht, the Netherlands; [f]Department of Cancer Immunology and Virology, Dana-Farber Cancer Institute, Boston, Massachusetts, USA; [g]Department of Radiology, Brigham and Women's Hospital, Harvard Medical School, Boston, Massachusetts, USA; [h]Centro Nacional de Investigaciones Cardiovasculares, Madrid, Spain; [i]Department of Radiology, Washington University, St Louis, Missouri, USA; [j]Department of Radiology, Memorial Sloan Kettering Cancer Center, New York, New York, USA; [k]Center for Systems Biology, Massachusetts General Hospital Research Institute and Department of Radiology, Harvard Medical School, Boston, Massachusetts, USA; [l]Cardiovascular Research Institute, Icahn School of Medicine at Mount Sinai, New York, New York, USA; [m]Department of Biomedical Engineering and Physics, Amsterdam Cardiovascular Sciences, Amsterdam UMC, University of Amsterdam, Amsterdam, the Netherlands; [n]Icahn Genomics Institute, Icahn School of Medicine at Mount Sinai, New York, New York, USA; and the [o]Department of Chemical Biology, Eindhoven University of Technology, Eindhoven, the Netherlands.

Frank Bengel, MD, served as Guest Associate Editor for this paper. Michael Bristow, MD, PhD, served as Guest Editor-in-Chief for this paper.

The authors attest they are in compliance with human studies committees and animal welfare regulations of the authors' institutions and Food and Drug Administration guidelines, including patient consent where appropriate. For more information, visit the Author Center.

Manuscript received June 22, 2022; revised manuscript received December 29, 2022, accepted December 29, 2022.

myocardial infarction. So far, research using temporary occlusion models has mainly focused on the paradoxically deteriorating effects of reperfusion on the myocardium, but not on systemic and immunologic processes.[7] Longitudinal read-outs that provide systemic information must be developed to comprehensively profile immune responses following temporal coronary artery occlusion and assess differences from those after permanent occlusion.[8] Although conventional ex vivo snapshot techniques offer vital information, they do not yield this level of insight. In vivo imaging methods such as magnetic resonance imaging (MRI) and positron emission tomography (PET) have the ability to fill this void.[9]

In the present study, we developed, validated, and applied multiparametric imaging methods to investigate the immune response following permanent and transient coronary artery occlusion. Specifically, we used different imaging modalities to profile distinct facets of the immune response after myocardial ischemia. We explored systemic immune activation and local leukocyte recruitment into the myocardium with the use of a combination of contrast-enhanced and fluorine MRI. In addition, we applied PET imaging approaches that report on immune cell metabolism, proliferation, and migration. Finally, we evaluated how different models of myocardial ischemia affect atherosclerotic plaque progression and cardiac function in mice.

METHODS

MICE. Ten-week-old male C57BL/6J mice and 8-week-old male *Apoe*$^{-/-}$ mice (B6.129P2-*Apoetm*^{1Unc}/J) were purchased from The Jackson Laboratory. *Apoe*$^{-/-}$ mice were fed a Western diet (Harlan Teklad TD.88137, 42% of calories from fat) for 10 weeks. All animal experiments were performed in accordance with protocols approved by the Institutional Animal Care and Use Committee of the Icahn School of Medicine at Mount Sinai and followed the National Institutes of Health guidelines for animal welfare.

MYOCARDIAL INFARCTION SURGERIES. Age-matched mice underwent permanent or temporary ligation of the left anterior descending coronary artery (LAD) to induce myocardial infarction. Anesthesia was induced with ketamine (100 mg/kg) and xylazine (10 mg/kg) intraperitoneally and maintained with isoflurane after intubation. Body temperature was held at 37 °C. Analgesia was provided with buprenorphine (0.1 mg/kg) before and 12 hours after surgery. After thoracotomy of the left fourth intercostal space, a retractor was used to keep the surgical field exposed. Next, pericardiotomy was performed, and the LAD was identified and then ligated with an 8-0 Prolene suture. Temporary ligation was maintained for 40 minutes via a small tube between the ligation suture and the LAD.[10] Sham procedure was executed the same way but without ligation of the LAD. Mice were extubated after the thoracotomy, and the skin was closed with sutures. C57BL/6J survival analysis included 29 mice with permanent LAD occlusion and 26 mice with temporary LAD occlusion. *Apoe*$^{-/-}$ survival analysis included 23 with permanent LAD occlusion and 25 with temporary LAD occlusion.

FUNCTIONAL AND LATE GADOLINIUM ENHANCEMENT CARDIAC MRI. Cardiac function and infarct size in isoflurane-anesthetized (4% for induction, 1% for maintenance) mice were assessed by means of cardiac MRI, using a 7.0-T small-animal scanner (Bruker BioSpec 70/30) equipped with a 40-mm-diameter $^{1}H/^{19}F$ volume coil (MR Coils). Cardiac MRI was performed 1 day after surgery for C57BL/6J mice and 2 days after surgery for *Apoe*$^{-/-}$ mice. Before being placed in the MRI scanner, mice were intraperitoneally injected with 0.4 mL/kg gadolinium contrast (Gadovist, Bayer). After survey scans to plan a cardiac short-axis orientation, 7 short-axis slices covering the heart from apex to base were scanned with a self-gated Cine 2D Flash sequence. This scan could be used to assess cardiac function and late gadolinium enhancement (LGE) infarct size. Sequence parameters were: repetition time (TR) = 10.5 ms; echo time (TE) = 1.9 ms; flip-angle = 20°; field-of-view (FOV) = 30 × 30 mm^2; slice thickness = 1 mm; acquisition matrix = 192 × 192; reconstruction matrix = 256 × 256; number of cardiac frames = 12; acquisition time = 4 minutes, 13 seconds per slice. The area of LGE uptake in percentage of the left ventricle and the left ventricular ejection fraction (LVEF) were analyzed with the use of Osirix MD (v12.0, Pixmeo) with the MRheart plugin in 5 to 7 cardiac short-axis slices, from apical to basal.

^{19}F-MRI. Formulating the PERFECTA nanotracer. PERFECTA, or 1,3-bis[[1,1,1,3,3,3-hexafluoro-2-(trifluoromethyl)propan-2-yl]oxy]-2,2-bis[[1,1,1,3,3,3-hexafluoro-2-2(trifluoromethyl)propan-2-yl]oxymethyl] propane, was synthesized as previously reported.[11] 1,2-Dimyristoyl-*sn*-glycero-3-phosphocholine (59 mg, 87 μmol; Avanti Polar Lipids) and 1-myristoyl-2-hydroxy-*sn*-glycero-3-phosphocholine (41 mg, 58 μmol; Avanti Polar Lipids) were dissolved in chloroform (2 mL). The solution was added dropwise to hot phosphate-buffered saline solution (PBS) (10 mL, 80 °C) and the obtained off-white suspension was stirred for 5 minutes before being allowed to cool to room temperature. If needed, additional PBS was added to attain a total volume of

10 mL. The resulting lipid suspension was stored at 4 °C for no more than 2 weeks. A mixture of the lipid suspension (0.5 mL), PBS (4.5 mL), and PERFECTA (100 mg, 0.10 mmol) was heated to approximately 80 °C in a glass vial by means of a microwave oven and directly afterward sonicated for 15 minutes with the use of a 150 V/T ultrasonic homogenizer equipped with a microtip working at 30% power output. The milky solution was allowed to cool to room temperature. Apolipoprotein-A1 (0.5 mg, purified in house from human high-density-lipoprotein obtained from Bioresource Technology) was added, and the mixture was incubated at room temperature for 12 to 16 hours. The mixture was shaken and subsequently left undisturbed for 30 seconds. Any precipitate was discarded, and the remaining suspension was transferred to a centrifugal filtration tube (1 MDa molecular weight cutoff; Vivaspin Sartorius Stedim Biotech). The tube was spun at 4,000*g* and 4 °C until concentrated to approximately 0.5 mL. Any precipitate was resuspended by repeatedly drawing the suspension up and down a pipette. PBS (5.0 mL) was added, and the solution was again concentrated to 0.5 mL and resuspended to produce the finished PERFECTA nanotracer. The nanotracer was diluted with PBS and injected intravenously via the tail vein at a concentration of 0.5 mg/g body weight, with typical injection volumes being around 100 μL. If not used immediately, the nanotracers were stored in the dark at 4 °C for a maximum of 2 weeks.

Physicochemical characterization of PERFECTA nanotracers. To determine particle size, an aliquot (10 μL) of the PERFECTA nanotracer suspension was diluted in PBS (1.0 mL) and analyzed by dynamic light scattering (DLS) to determine the mean of its number and average size distribution. DLS measurements were performed on a NanoBrook ZetaPlus system (Brookhaven Instruments). The typical particle size was 182 ± 15 nm; n = 7. PERFECTA concentrations were determined by means of ^{19}F nuclear magnetic resonance spectroscopy (NMR). A suspension of nanotracers (90 vol%) and deuterium oxide (10 vol%) containing a predetermined amount of sodium trifluoroacetate as an internal standard was prepared. Samples of the suspension were analyzed by means of ^{19}F-NMR with the use of a Bruker 600 Ultrashield magnet connected to a Bruker Avance 600 console. Data were processed with the use of Topspin v.3.5pl7. Typical PERFECTA nanotracer concentrations were around 150 mg/mL.

^{19}F-MRI protocol. In vivo ^{19}F-MRI was performed in the same scanning session and with the same setup described above for MRI of cardiac function and LGE. To obtain an anatomic background, we first acquired a ^{1}H whole-body 3D fast imaging with steady-state precession scan with the following parameters: TR = 8 ms; TE = 4 ms; flip-angle = 15°; FOV = 64 × 32 × 32 mm^2; acquisition matrix = 256 × 96 × 9six, reconstruction matrix = 256 × 128 × 128; number of signal averages (NSA) = 4; acquisition time = 4 minutes 54 seconds. Whole-body ^{19}F-MRI was performed with a 3D rapid acquisition with relaxation enhancement (RARE) sequence with the following parameters: TR = 1,000 ms; TE = 10.9 ms; RARE factor = 16; FOV = 64 × 32 × 32 mm^2; acquisition matrix = 128 × 64 × 64; reconstruction matrix = 128 × 64 × 64; NSA = 6; acquisition time = 25 minutes 36 seconds. Next, a higher-resolution 3D RARE ^{19}F scan of the heart was conducted in the same short-axis orientation as the ^{1}H Cine cardiac scans and with the following parameters: TR = 1,000 ms; TE = 8 ms; RARE factor = 16; FOV = 30 × 30 × 16 mm^2; acquisition matrix = 64 × 64 × 16; reconstruction matrix = 64 × 64 × 16; NSA = 32; acquisition time = 34 minutes 8 seconds.

Image analysis. The target-to-background ratio (TBR) was calculated, with the use of Osirix MD (v12.0, Pixmeo), for fluorine uptake in the infarct area and spleen. LVEF and LGE as percentage of the left ventricle were analyzed as described above. Fluorine uptake in the infarct area was calculated from the LGE area as target zone in all 5 to 7 cardiac short-axis slices and upper limb muscles as background. The spleen TBR was measured by using the whole spleen in the abdominal ^{1}H coronal images as the target area and using the psoas muscle as the background area. After image fusion of ^{1}H/^{19}F, the TBR was calculated.

PET/CT IMAGING. Before the PET/computed tomographic (CT) scan, animals were anesthetized with an isoflurane (Baxter Healthcare)-oxygen gas mixture (4% for induction, 1% for maintenance) and subsequently imaged on a nano PET/CT scanner (Mediso). A tail vein catheter was inserted and contrast (Isovue-370; Bracco Diagnostics) was injected at a rate of 0.5 mL/min. A whole-body CT scan was performed (energy 50 kVp, current 180 μAs, isotropic voxel size 0.25 mm^3), followed by a PET scan. The coincidences were filtered with an energy window 400-600 keV. The voxel size was isotropic and 0.6 mm^3 in width, and the reconstruction was applied for 2 complete iterations, with 6 subsets per iteration. PET data were reconstructed using CT-based attenuation correction. Reconstruction was performed with the TeraTomo 3D reconstruction algorithm from Mediso Nucline software.

Fluorothymidine PET. ^{18}F-Fluorothymidine (FLT) was synthesized as reported previously.[12] Briefly, ^{18}F

was eluted in 4,7,13,16,21,24-hexaoxa-1,10-diazabicyclo[8.8.8]hexacosane, K_2CO_3, and MeCN. Solvents were removed azeotropically and 3-N-Boc-5′-O-dimethoxytrityl-3′-O-nosyl-thymidine in dry acetonitrile was added. N-Hydrochloric acid was then added to the mixture, followed by sodium acetate neutralization. Two days after myocardial infarction of C57BL/6 mice, ^{18}F-FLT (382 ± 20.3 μCi in 100 μL PBS) was administered via the tail vein and allowed to circulate for 90 minutes before PET imaging (30 minutes acquisition time).

Fluorodeoxyglucose PET. Two days after myocardial infarction, C57BL/6 mice were fasted overnight before ^{18}F-fluorodeoxyglucose (FDG) (340 ± 27.0 μCi in 100 μL PBS solution) injection, which was administered via the tail vein and allowed to circulate for 30 minutes before PET imaging (30 minutes acquisition time).

CD11b PET. CD11b-specific nanobodies were purified from *Escherichia coli* WK6 cells through immobilized metal affinity chromatography with the use of Ni-NTA beads, followed by functionalization with the chelator deferoxamine (DFO). The DFO-functionalized nanobody was then PEGylated, radiolabeled with ^{89}Zr in chelexed PBS and purified with the use of a PD-10 size exclusion cartridge. The purification and radiolabeling process is described elsewhere in more detail.[13] The radiochemical purity was >97%. Two days after myocardial infarction, C57BL/6 mice were injected with ^{89}Zr-labeled CD11b-specific nanobodies (200 ± 17.5 μCi in 100 μL PBS) via the tail vein. PET imaging was performed 24 hours later (30 minutes acquisition time).

C-C motif chemokine receptor 2 PET. ^{64}Cu-1,4,7,10-tetraazacyclododecane-1,4,7,10-tetraacetic acid (DOTA)-extracellular loop 1 inverso (ECL1i) that allosterically binds to C-C motif chemokine receptor 2 (CCR2) was generously given to us by Dr Gropler (Washington University, St Louis, MO) as an intact radiotracer. ECL1i peptide was synthesized from D-form amino acids obtained from CPC Scientific, and maleimide-mono-amide-DOTA was purchased from Macrocyclics. The complete description of DOTA-ECL1i synthesis and radiolabeling with ^{64}Cu was reported previously.[14-16] The radiochemical purity was more than 95% (determined by radio-HPLC) before administration to mice. Two days after myocardial infarction, C57BL/6 mice received ^{64}Cu-DOTA-ECL1i (354 ± 65.8 μCi in 100 μL PBS) via tail vein injection and a 0- to 60-minute dynamic PET scan was performed.

Image analysis. Whole-body CT images of mice were fused with PET images (Osirix MD v12.0, Pixmeo) and analyzed along a coronal axis. Regions of interest (ROIs) were drawn on the CT image over tissues of interest, with 1 ROI drawn at every fourth coronal slice. After drawing ROIs, the remaining slices were interpolated with the use of OsirixMD's "generate missing ROIs" feature. The spleen and femur were drawn in their entirety, and samples of 3 lumbar vertebrae were used for spinal bone marrow. For the (infarcted) myocardium, ROIs were drawn axially on the anterior wall of the left ventricle in every slice from the apex moving cranially to approximately three-fourths of the height of the left ventricle. For remote myocardium, ROIs were drawn axially on the left ventricle wall at the opposite side of the infarct. In noninfarcted animals, ROIs were drawn in the same locations. ROI mean standardized uptake values (SUVs) were calculated by transferring ROIs to the SUV-converted PET image. ROI SUVs of each organ were then exported to a CSV file, and SUVs were averaged for each organ.

EX VIVO GAMMA COUNTING. Immediately after the PET scans, animals were euthanized and perfused with PBS, tissues of interest (remote myocardium, infarcted myocardium, corresponding myocardium of control animals, spleen, and femoral bone marrow) were collected and weighed in preweighed tubes. Radioactivity content was measured with the use of a Wizard2 2480 automatic gamma counter (Perkin Elmer). Tissue radioactivity concentration was calculated, decay corrected, and expressed as percentage of the injected dose per gram of tissue (%ID/g).

FLOW CYTOMETRY. For flow cytometry analysis, blood was obtained by cardiac puncture and collected in an EDTA-coated tube. Mice were subsequently perfused through the left ventricle with 10 mL cold PBS. Femur and spleen were collected. The infarcted heart tissue was collected and weighed. In *Apoe*$^{-/-}$ mice, the aorta, from the aortic root to the iliac bifurcation, was also collected. Absolute cell counting was performed by adding CountBright beads (Invitrogen) to each sample and calculating the ratio of bead events to cell events. Data were acquired with an LSRFortessa flow cytometer (BD Biosciences) and were analyzed with the use of FlowJo v10.7.1.

Heart and aorta processing and analysis. The aorta was minced and digested by means of an enzymatic digestion solution containing liberase TH (4 U/mL; Roche), DNase I (40 U/mL; Sigma-Aldrich), and hyaluronidase (60 U/mL; Sigma-Aldrich) in PBS. Heart tissue was minced and digested with the use of an enzymatic digestion solution containing DNase I (60 U/mL), collagenase type I (450 U/mL), collagenase type XI (125 U/mL), and hyaluronidase (60 U/mL) (all

JACC: BASIC TO TRANSLATIONAL SCIENCE VOL. 8, NO. 7, 2023
JULY 2023:801–816

from Sigma-Aldrich) in PBS. Aortas and heart tissues were incubated for 1 hour at 37 °C under agitation. Cells were filtered through a 70-μm cell strainer and washed with fluorescence-activated cell sorting (FACS) buffer (Dulbecco's PBS with 1% fetal calf serum, 0.5% bovine serum albumin, 0.1% NaN_3, and 1 mmol/L EDTA). Single-cell suspensions were stained with the following monoclonal antibodies: PE anti-mouse/human CD11b (clone M1/70, 1:200; BioLegend), PE-Cy7 anti-mouse F4/80 (clone BM8, 1:100; BioLegend), FITC anti-mouse Ly6C (clone AL-21, 1:400; BD Biosciences), BV510 anti-mouse CD45 (clone 30-F11, 1:200; BioLegend) and a lineage cocktail (Lin) containing eFluor 450 anti-mouse CD90.2 (clone 53-2.1, 1:200; eBioscience), eFluor 450 anti-mouse TER-119 (clone TER-119, 1:200; eBioscience), eFluor 450 anti-mouse NK-1.1 (clone PK136, 1:200; eBioscience), eFluor anti-mouse CD49b (clone DX5, 1:200; eBioscience), eFluor 450 anti-mouse/human CD45R/B220 (clone RA3-6B2, 1:200; eBioscience), eFluor 450 anti-mouse CD103 (clone 2E7, 1:200; eBioscience), and eFluor 450 anti-mouse Ly-6G (clone 1A8, 1:100; eBioscience); 10 μL DAPI was added for viability staining. CD11b+ cells were identified as $CD45^+$ $CD11b^+$, and Lin.$^-$ Monocytes were identified as CD45+, $CD11b^{high}$, $Lin^{-/low}$, and $Ly6C^{high/low}$. Neutrophils were identified as CD45+, $CD11b^{high}$, and Lin^+. Macrophages were identified as CD45+, $CD11b^{high}$, $Lin^{-/low}$, and $F4/80^{high}$.

Blood processing and analysis. Blood was incubated with red blood cell lysis buffer for 4 minutes and washed with FACS buffer; this was repeated twice more. Single-cell suspensions were stained with the following monoclonal antibodies: APC anti-CD115 (clone AFS98, 1:200; eBiosciences), PerCP-Cy5.5 anti-CD11b (clone M1/70, 1:200; BioLegend), PE-Cy7 anti-Ly6C (clone Al-21, 1:200; BioLegend), eFluor 450 anti-Ly6G (clone 1A8, 1:100; eBioscience), anti-CD19 (clone 1D3, 1:400; BD Pharmingen) and anti-CD90.2 (clone 53-2.1, 1:400; BD Pharmingen); 10 μL DAPI was added for viability staining. $CD11b^+$ cells were identified as $CD11b^+$ and Lin^-. Neutrophils were identified as $CD11b^{high}$, $Lin^{-/low}$, $CD115^{low}$, and $Ly6G^{high}$. Monocytes were identified as $CD11b^{high}$, $Lin^{-/low}$, $CD115^{high}$, and $Ly6C^{high/low}$.

Progenitors and progenitor proliferation. For BrdU labeling, C57BL/6 mice were intraperitoneally injected with 1 mg BrdU (10 mg/mL in PBS) 2 days after myocardial infarction and euthanized 24 hours later. Bone marrow was flushed out of the femur with PBS, filtered through a 70-μm cell strainer, incubated with lysis buffer for 30 seconds, and washed with FACS buffer. Cells were stained with APC/Cy7 anti-CD48 (clone HM48-1, 1:80; BioLegend), PerCP/Cy5.5 anti-CD150 (clone TC15-12F12.2, 1:160; BioLegend), PE anti-CD117 (c-Kit, clone 2B8, 1:400; BioLegend), anti-Sca-1 (Ly6-A/E, clone E13-161.7, 1:160; BioLegend), and a lineage cocktail (1:10; BD Biosciences) containing anti-CD3ε (clone 500A2), anti-CD11b (clone M1/70), anti-CD45R/B220 (clone RA3-6B2), anti-Ly76 (clone TER-119), and anti-Ly6G/Ly6C (clone RB6-8C5). BrdU staining was performed with the use of the BrdU staining kit (BD FITC BrdU Flow Kit; Fisher Scientific), following the manufacturer's instructions. LSK cells were identified as Lin^-, $Sca\text{-}1^+$, and $c\text{-}Kit^+$.

HISTOLOGY OF AORTIC ROOTS. Aortic roots were harvested from *Apoe*$^{-/-}$ mice, embedded in OCT (Sakura Finetek), and frozen. Sections 5 μm thick were stained with rat anti-MAC3 antibody (clone M3/84, 1:100; BD Biosciences) followed by a biotinylated antirat secondary antibody (1:300; Vector Laboratories). Vecta Stain ABC kit and ImmPact vector red (both from Vector Laboratories) were used for color development. Next, counterstaining with hematoxylin was carried out. Total plaque size and $mac3^+$ area were analyzed with the use of ImageJ (v2.1.0/1.53c) by taking the average of 6 sections spaced ∼30 μm apart, beginning at the base of the aortic root.

STATISTICS. Data are presented as mean ± SEM. Statistical analyses were performed with Prism 9 (GraphPad Software). First, normal distribution tests were carried out (d'Agostino and Pearson test, Anderson-Darling test, Shapiro-Wilk test, Kolmogorov-Smirnov test). Student's *t*-test for 2 groups or 1-way analysis of variance (ANOVA) for more than 2 groups was used if data passed the normal distribution tests. If data failed the normal distribution tests, the Mann-Whitney test for 2 groups or the Kruskal-Wallis test (uncorrected Dunn's test) for more than 2 groups was performed. We computed nonparametric Spearman correlations to evaluate the relation between tracer uptake in different tissues of interest. We used Pearson correlation coefficients for infarct ^{19}F-MRI TBR and LVEF. Survival evaluation was conducted by means of simple Kaplan-Meier analysis. Values of $P < 0.05$ were considered to be significant. Statistical tests and animal numbers for each graph are specified in the figure legends.

RESULTS

ISCHEMIA-REPERFUSION AND PERMANENT LAD OCCLUSION RESULT IN DISTINCT MYOCARDIAL INJURY AND CARDIAC FUNCTION PROFILES. We profiled the immune responses to cardiac ischemia

FIGURE 1 **IR and PO Result in Distinct Myocardial Injury and Cardiac Function Profiles**

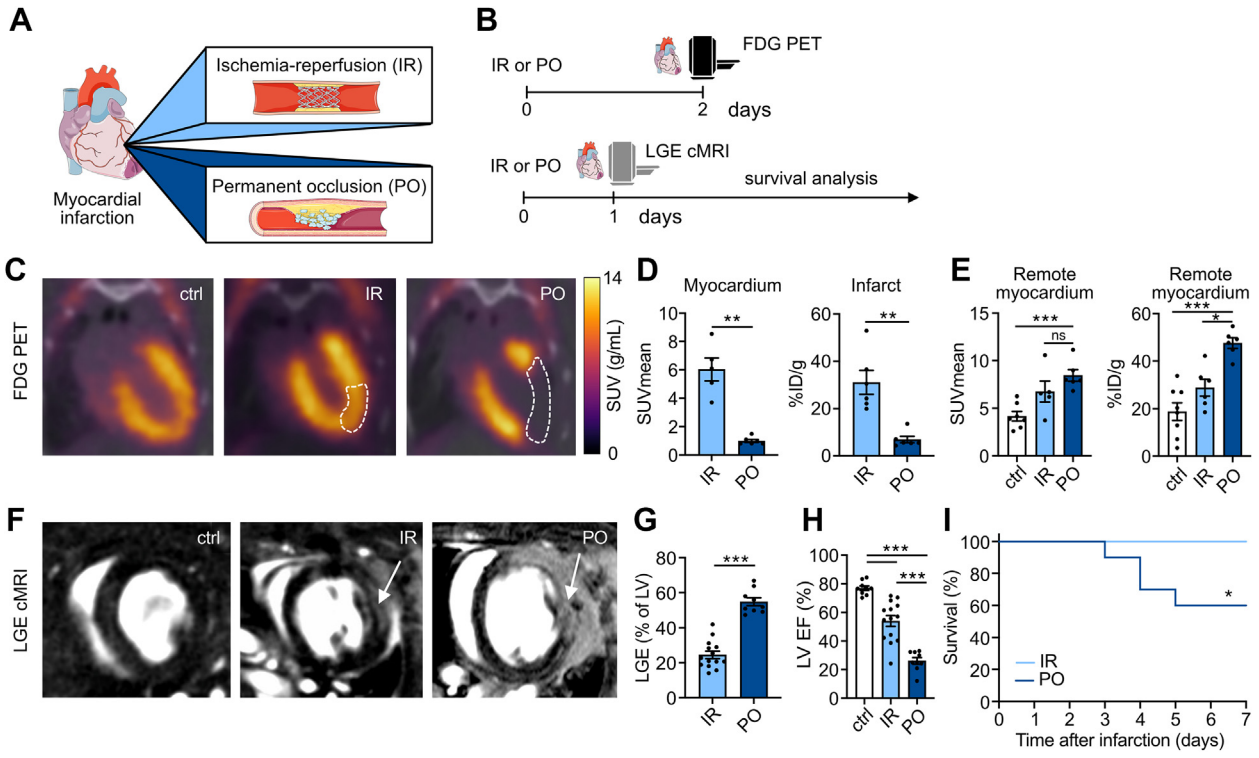

(A) This study compared mouse models of ischemia -reperfusion (IR) injury, with 40 minutes of ischemia, and permanent left anterior descending coronary artery occlusion (PO). **(B)** We performed ^{18}F-fluorodeoxyglucose (FDG) PET imaging 2 days after IR or PO surgery. Late gadolinium enhancement (LGE) cardiac MRI was performed 1 day after IR or PO surgery, followed by survival analysis for 1 week. **(C)** FDG PET/CT 2 days after surgery allowed accurate delineation of the infarct zone. **Dashed lines** highlight the infarct area. **(D)** ^{18}F-FDG uptake as mean standardized uptake values (SUVs) of the infarct area and as % injected dose (ID)/g infarct tissue (n = 5-6; $P = 0.004$ for SUVmean; $P = 0.002$ for %ID/g; 2-tailed Mann-Whitney test). **(E)** ^{18}F-FDG uptake in the remote myocardium of mice with PO and IR and the corresponding healthy myocardium of control mice (SUVmean: n = 5-7, $P = 0.001$ control vs PO, $P = 0.132$ IR vs PO; %ID/g: n = 5-8, $P = 0.025$ IR vs PO, $P < 0.001$ control vs PO; Kruskal-Wallis test). **(F)** Representative LGE cardiac MRI; **arrows** indicate infarct area. **(G)** LGE area in % of left ventricle (n = 9-14; $P < 0.001$; 2-tailed Student's *t*-test). **(H)** Left ventricular ejection fraction (LVEF) in % for control, IR, and PO mice (n = 9-14; $P < 0.001$ for IR vs PO, ctrl vs IR, control vs PO; 1-way ANOVA). **(I)** Simple survival analysis for IR and PO mice for 1 week after myocardial infarction induction (n = 26-29; log-rank test: $P = 0.015$). Data are presented as mean ± SEM, unless otherwise specified. *P <0.05; **P <0.01; ***P <0.001. ANOVA = analysis of variance; MRI =magnetic resonance imaging.

using two different myocardial infarction models (see Supplemental Figure 1a for an overview of the entire study). Male C57BL/6 mice underwent either 40-minute occlusion of the LAD, followed by reperfusion (ischemia-reperfusion, IR), or permanent ligation (permanent occlusion, PO) of the same coronary artery (**Figure 1A**).

First, we used in vivo imaging to investigate differences in cardiac pathology between the IR and PO models. Specifically, we used ^{18}F-FDG PET to assess cardiac viability and MRI to evaluate cardiac function and infarct size (**Figure 1B**). Two days after cardiac ischemia, mice with permanent LAD occlusion showed significantly less ^{18}F-FDG uptake in the ischemic myocardium than mice with temporary LAD occlusion, as assessed by in vivo PET imaging and ex vivo gamma counting (**Figures 1C and 1D**). We observed compensatory higher ^{18}F-FDG uptake in the remote myocardium of mice with permanent coronary artery occlusion, compared with mice with IR injury and control mice (**Figure 1E**). LGE cardiac MRI 1 day after the ischemic event delineated cardiac function and necrosis with high accuracy (**Figure 1F**). We observed ~2.5-fold larger infarcts after PO compared with IR (**Figure 1G**), resulting in strongly impaired LVEF in mice with PO. In contrast, mice with IR had relatively preserved LVEF (**Figure 1H**). These results were consistent on day 6 after the ischemic event (Supplemental Figures 1b to 1d). Consequently, mice with reperfusion intervention had better survival than mice without reperfusion salvage (**Figure 1I**). Collectively, and in line with

FIGURE 2 **Ischemia Severity Dictates Myeloid Cell Influx Into the Ischemic Myocardium**

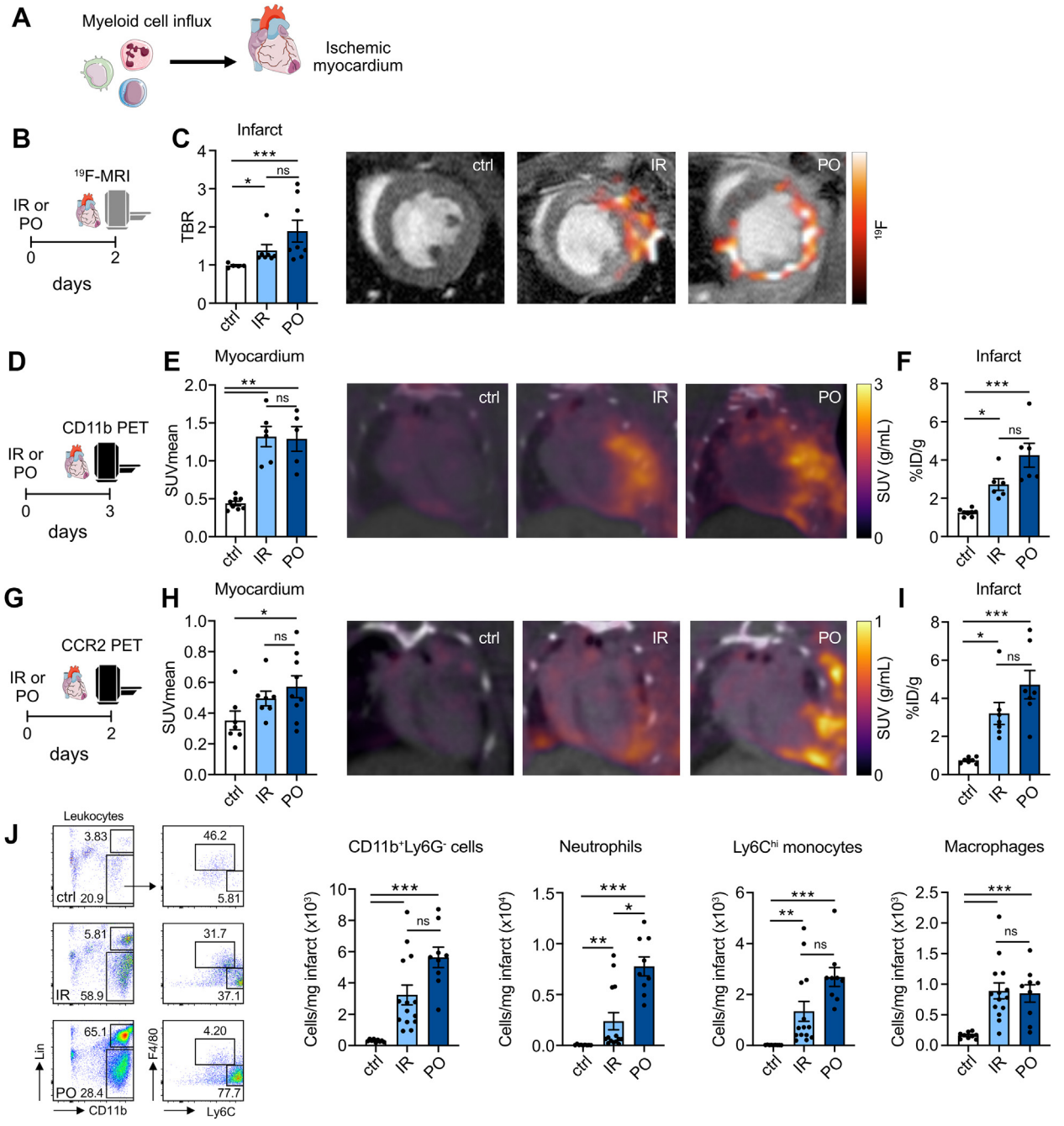

Continued on the next page

previous studies,[17-19] our experiments detected profound differences in myocardial injury and cardiac function between the two myocardial infarction models.

ISCHEMIA SEVERITY CORRELATES WITH IMMUNE CELL ACCUMULATION IN THE INFARCTED MYOCARDIUM. We next studied whether these substantially different cardiac outcomes are accompanied by distinct

leukocyte infiltration profiles in the infarcted tissue (Figure 2A). To this end, we first used lipoprotein-based nanomaterials, which can be used as in vivo immune cell tracers owing to their inherent propensity for myeloid cell uptake,[20] which we loaded with perfluorocarbons (Supplemental Figure 2a). Perfluorocarbons are biologically inert and can be imaged by ^{19}F-MRI with high specificity owing to a negligible in vivo background signal.[21-23] We used the perfluorocarbon PERFECTA, a compound that has 36 equivalent fluorine atoms and thus enables highly sensitive ^{19}F-MRI applications.[11] We intravenously injected our PERFECTA nanotracer 1 day after myocardial infarction and performed ^{19}F-MRI of the myocardium the following day to investigate myeloid cell recruitment to the infarct (Figure 2B). Mice with IR and PO had significantly higher ^{19}F signal compared with control mice ($P = 0.021$ control vs IR; $P < 0.001$ control vs PO) (Figure 2C), suggesting myeloid cell influx. We observed a weak inverse correlation between ^{19}F infarct signal and cardiac function (Supplemental Figure 2b).

In addition, we performed PET imaging of the myeloid cell burden in the heart with the use of an ^{89}Zr-labeled CD11b-specific nanobody. This PET tracer is based on single-domain antibody fragments targeting the CD11b cell surface antigen, which is expressed by neutrophils, monocytes, and macrophages,[24,25] and was initially developed and successfully applied in preclinical cancer imaging.[26,27] To study CD11b expression in the infarct zone, we injected the radiotracer 2 days after cardiac ischemia and performed PET imaging 24 hours later (Figure 2D). CD11b-specific nanobody PET imaging detected 3-fold higher uptake in the infarct zones of IR and PO mice compared with the same cardiac region of noninfarcted mice ($P = 0.002$ control vs IR; $P = 0.002$ control vs PO) (Figure 2E). Ex vivo gamma counting confirmed significantly enhanced ^{89}Zr uptake in the ischemic myocardium, indicating higher CD11b$^+$ cell burden than in myocardium of control mice ($P = 0.019$ control vs IR; $P < 0.001$ control vs PO) (Figure 2F).

To investigate inflammatory monocyte recruitment to the infarct area, we applied ^{64}Cu-DOTA-ECL1i PET imaging of C-C motif chemokine receptor 2 (CCR2) (Figure 2G). Expression of this receptor is required for monocyte migration to inflammatory lesions.[28] This radiotracer has previously been used to image CCR2 expression in several preclinical animal models as well as in patients with pulmonary fibrosis.[29-31] CCR2 PET imaging of the two myocardial infarction models revealed increased signal in the infarct area of mice subjected to PO compared with control mice ($P = 0.021$) (Figure 2H). In addition, ex vivo gamma counting showed more activity in the infarct zones of both myocardial infarction models than in myocardium of control mice ($P = 0.011$ control vs IR; $P < 0.001$ control vs PO) (Figure 2I).

Two days after infarction, we performed flow cytometry analysis of the infarcted myocardium in both models to further validate our imaging findings. In agreement with the imaging findings, we found significantly increased CD11b$^+$ cell numbers in the myocardial infarction models than in control mice ($P < 0.001$ control vs IR; $P < 0.001$ control vs PO; $P = 0.092$ IR vs PO) (Figure 2J, Supplemental Figure 3a). When comparing the two infarction models, we found more neutrophils in the infarct zone after PO than after IR ($P = 0.027$). In addition, we observed a trend toward

FIGURE 2 Continued

(A) Myeloid cell influx to the ischemic myocardium assessed by multimodal imaging. **(B)** ^{19}F-MRI of the heart 2 days after IR/PO surgery and 1 day after PERFECTA nanotracer injection. **(C)** ^{19}F concentration in the infarct zone of PO mice compared with IR and control mice, expressed as target-to-background ratio (TBR; n = 5-8; $P = 0.021$ for control vs IR; $P < 0.001$ for ctrl vs PO; $P = 0.22$ IR vs PO; Kruskal-Wallis test). Fused ^{19}F-MRI with fluorine uptake in the infarct zone. **(D)** CD11b PET was performed 3 days after IR/PO surgery and 2 days after tracer injection. **(E)** CD11b PET signal quantification expressed as SUVmean (n = 5-8; $P = 0.002$ control vs IR; $P = 0.002$ control vs PO; $P = 0.91$ IR vs PO; Kruskal-Wallis test) and fused PET/CT images of the heart. **(F)** Ex vivo quantification showed higher tracer uptake for mice with IR and PO injury compared to control mice (n = 6-8; $P = 0.019$ control vs IR; $P < 0.001$ control vs PO; $P = 0.14$ IR vs PO; Kruskal-Wallis test). **(G)** CCR2 PET to image inflammatory monocytes was performed 2 days after IR/PO surgery. The scan occurred during the first 60 minutes after ^{64}Cu-DOTA-ECL1i injection. **(H)** ^{64}Cu-DOTA-ECL1i PET signal quantification expressed as SUVmean (n = 7-9; $P = 0.083$ control vs IR; $P = 0.021$ control vs PO; $P = 0.64$ IR vs PO; Kruskal-Wallis test) and representative images of control, IR, and PO mice. **(I)** Ex vivo quantification of tracer uptake by gamma-counting (n = 7; $P = 0.011$ control vs IR; $P < 0.001$ control vs PO; $P = 0.21$ IR vs PO; Kruskal-Wallis test). **(J)** Flow cytometry of the infarct zone 2 days after myocardial infarction. **(Left)** Representative flow plots for control, IR and PO hearts, gated on leukocytes. **(Right)** Quantification of CD11b$^+$/Ly6G$^-$ cells (n = 9-14; $P < 0.001$ control vs IR; $P < 0.001$ control vs PO; $P = 0.092$ IR vs PO; Kruskal-Wallis test), neutrophils (n = 9-14; $P = 0.002$ control vs IR; $P < 0.001$ control vs PO; $P = 0.028$ IR vs PO; Kruskal-Wallis test), Ly6C^{high} monocytes (n = 9-14; $P = 0.001$ control vs IR; $P < 0.001$ control vs PO; $P = 0.069$ IR vs PO; Kruskal-Wallis test), and macrophages (n = 9-14; $P < 0.001$ control vs IR; $P < 0.001$ control vs PO; $P = 0.87$ IR vs PO; Kruskal-Wallis test) in the infarct. Data are presented as mean ± SEM, unless otherwise specified. *P <0.05; **P <0.01; ***P <0.001. Abbreviations as in Figure 1.

elevated Ly6C^{high} monocyte numbers in the PO group ($P = 0.069$), whereas macrophage numbers were similar in both models 2 days after infarction. Seven days after inducing cardiac ischemia, we detected a difference between PO and IR regarding macrophage burden in the infarct (Supplemental Figure 3b). Overall, flow cytometry data for the infarct area align with our imaging results and indicate distinct differences in immune response severity.

Next, we investigated the relationship between cardiac function (as assessed by cMR) and myeloid cell burden in the infarct area (as measured by flow cytometry), and we noted a strong inverse correlation between these parameters (Supplemental Figure 3c). Taken together, these results demonstrate that the two models of cardiac ischemia differ in their degree of inflammatory cell infiltration into the infarct zone and that these infiltration levels negatively correlate with cardiac function.

BONE MARROW RESPONSES ARE SIMILAR IN ISCHEMIA-REPERFUSION AND PERMANENT OCCLUSION. The immune cells that infiltrate the heart are produced in the bone marrow and spleen and are quickly deployed from these organs.[3] In response to the inflammatory factors and damage-associated molecular patterns generated and released after myocardial ischemia, the proliferation of inflammatory immune cell progenitors profoundly increases before leukocyte release from the hematopoietic organs, a process called emergency hematopoiesis.[32] We used multimodal imaging to investigate potential differences in emergency hematopoiesis by measuring proliferation and metabolic activity in the bone marrow and myeloid cell egress from the hematopoietic tissues (**Figure 3A**).

We first assessed proliferation with the use of ^{18}F-fluorothymidine (FLT) PET 2 days after infarction (**Figure 3B**).^{18}F-FLT uptake in the bone marrow was significantly higher in both myocardial infarction mouse models compared with control animals, but there was no difference between the two models (**Figures 3C and 3D**). We complemented these findings with the use of flow cytometry to evaluate BrdU incorporation in bone marrow LSK hematopoietic stem and progenitor cells 3 days after infarction. We found significantly more BrdU-positive LSK cells in both myocardial infarction models compared with naïve control mice (**Figure 3E**, Supplemental Figure 4a). These data suggest that the increased hematopoietic proliferation does not depend on the type of cardiac ischemia.

Post-myocardial infarction emergency hematopoiesis is an energy-demanding process. We therefore used ^{18}F-FDG PET to investigate metabolic activity (**Figure 3F**). In line with data on proliferation, mice with either type of myocardial infarction displayed significantly higher ^{18}F-FDG accumulation in the bone marrow compared with control mice, although we observed no significant difference between IR and PO mice by means of either in vivo PET imaging or ex vivo gamma counting (**Figures 3G and 3H**). Correspondingly, we found more LSK cells in the bone marrow of the myocardial infarction groups compared with control mice ($P = 0.003$ control vs IR; $P = 0.052$ control vs PO) (**Figure 3I**), whereas there was no difference between IR and PO models.

We also used the CD11b PET imaging data to explore myeloid cell dynamics in the bone marrow. The radiotracer was injected 2 days after myocardial infarction, and imaging was performed 1 day later (ie, 3 days after cardiac ischemia) (**Figure 3J**). We found significantly lower bone marrow signal in the IR and PO mouse models than in control mice ($P = 0.001$ control vs IR; $P = 0.032$ control vs PO) (**Figures 3K and 3L**), suggesting myeloid cell egress. Corroboratively, we found increased CD11b^{+} cells in the circulation in both myocardial infarction models compared with naïve control mice ($P = 0.021$ control vs IR; $P = 0.025$ control vs PO) (**Figure 3M**, Supplemental Figure 4B), mainly driven by an expansion in circulating neutrophils ($P = 0.001$ control vs IR; $P = 0.003$ control vs PO) (Supplemental Figure 4C). We did not detect a difference in CCR2 expression in the bone marrow after myocardial infarction (Supplemental Figures 4D to 4F). Although more CCR2+ inflammatory cells are produced after myocardial infarction, their immediate departure from the bone marrow could explain the lack of alterations in PET signal.[33]

We also pursued multiparametric immunoimaging of the spleen. In line with the bone marrow data, we found slightly increased ^{18}F-FLT uptake in the spleen of PO mice compared with control mice ($P = 0.042$), and we observed no difference between the two myocardial infarction models (Supplemental Figures 5a to 5c). FDG PET imaging did not indicate altered metabolic activity in the spleen (Supplemental Figures 5d to 5f). After PERFECTA-nanotracer injection, ^{19}F-MRI signal decreased in the spleen only in PO mice, compared with control, suggesting myeloid cell egress ($P = 0.004$ control vs PO; $P = 0.015$ IR vs PO) (Supplemental Figures 5g and 5h). However, when we used ^{89}Zr-CD11b nanobodies to probe myeloid cell dynamics in the spleen, we found lower signal in both models than in control mice ($P = 0.041$ control vs PO; $P = 0.046$ control vs PO) (Supplemental Figures 5i to 5k). Ex vivo gamma counting revealed slightly elevated CCR2 expression

FIGURE 3 **Bone Marrow Activity After Cardiac Ischemia-Reperfusion and Permanent Left Anterior Descending Coronary Artery Occlusion Are Similar**

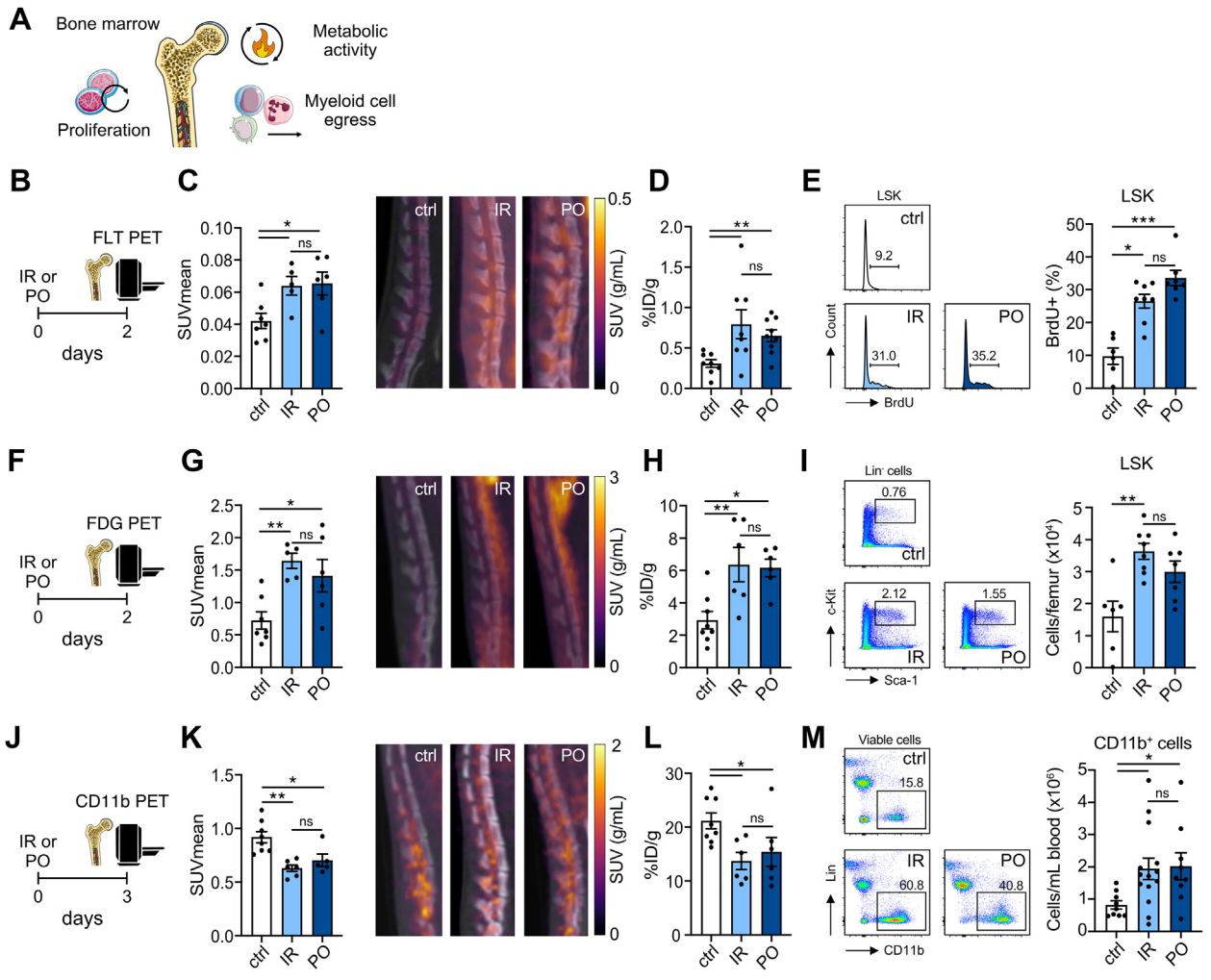

(A) Cardiac ischemia induces proliferation, metabolic activation, and myeloid cell egress in/from the bone marrow. We probed these processes via molecular imaging. **(B)** ^{18}F-fluorothymidine (FLT) PET/CT was performed 2 days after IR/PO surgery. ^{18}F-FLT was injected 90 minutes before the scan. **(C)** Quantification of ^{18}F-FLT signal in the lumbar vertebrae (n = 5-7; $P = 0.032$ control vs IR; $P = 0.018$ control vs PO; $P = 0.92$ IR vs PO; Kruskal-Wallis test) and representative ^{18}F-FLT PET/CT images showing higher activity for both IR and PO mice. **(D)** Ex vivo gamma counting of ^{18}F-FLT uptake in the bone marrow (n = 8-9; $P = 0.006$ control vs IR; $P = 0.006$ control vs PO; $P = 0.92$ IR vs PO; Kruskal-Wallis test). **(E)** Flow cytometry analysis of bone marrow cells 3 days after IR/PO. Representative histograms of BrdU expression in Lin$^-$Sca-1$^+$cKit$^+$ (LSK) cells and quantification of BrdU-positive cells. BrdU (1 mg) was injected i.*P.* 24 hours before analysis (n = 6-8, $P = 0.014$ control vs IR; $P < 0.001$ control vs PO; $P = 0.18$ IR vs PO; Kruskal-Wallis test). **(F)** ^{18}F-FDG PET/CT was performed 2 days after IR/PO surgery. ^{18}F-FDG was injected 30 minutes before imaging. **(G)** Quantification of ^{18}F-FDG signal in the lumbar vertebrae (n = 5-7; $P = 0.005$ control vs IR; $P = 0.025$ control vs PO; $P = 0.52$ IR vs PO; Kruskal-Wallis test) and representative images showing higher activity in IR and PO mice compared with control mice. **(H)** Ex vivo gamma counting of ^{18}F-FDG uptake in the bone marrow (n = 6-8; $P = 0.008$ control vs IR; $P = 0.011$ control vs PO; $P = 0.92$ IR vs PO; Kruskal-Wallis test). **(I)** Number of LSK cells in the bone marrow 3 days after IR/PO (n = 6-8; $P = 0.003$ control vs IR; $P = 0.052$ control vs PO; $P = 0.33$ IR vs PO; Kruskal-Wallis test) with representative plots. **(J)** CD11b PET was performed 3 days after myocardial infarction. The ^{89}Zr-labeled CD11b-specific nanobody was injected 2 days after myocardial infarction. **(K)** Quantification of PET signal in the lumbar vertebrae (n = 5-8; $P = 0.001$ control vs IR; $P = 0.032$ control vs PO; $P = 0.41$ IR vs PO; Kruskal-Wallis test) and representative images showing lower signal in mice with IR or PO surgery compared with control. **(L)** Ex vivo gamma counting of tracer uptake in the bone marrow (n = 6-8; $P = 0.017$ control vs IR; $P = 0.039$ control vs PO; $P = 0.77$ IR vs PO; Kruskal-Wallis test). **(M)** Representative flow plots of blood samples, gated on viable cells. Significantly higher numbers of CD11b$^+$ cells were observed in the blood of IR and PO animals 2 days after infarction (n = 9-14; $P = 0.021$ control vs IR; $P = 0.025$ control vs PO; $P = 0.87$ IR vs PO; 1-way ANOVA). Data are presented as mean ± SEM, unless otherwise specified. *P <0.05; **P <0.01, ***P <0.001. Abbreviations as in Figures 1 and 2.

FIGURE 4 Heatmap of Correlations Between Tracer Uptake in Tissues of Interest

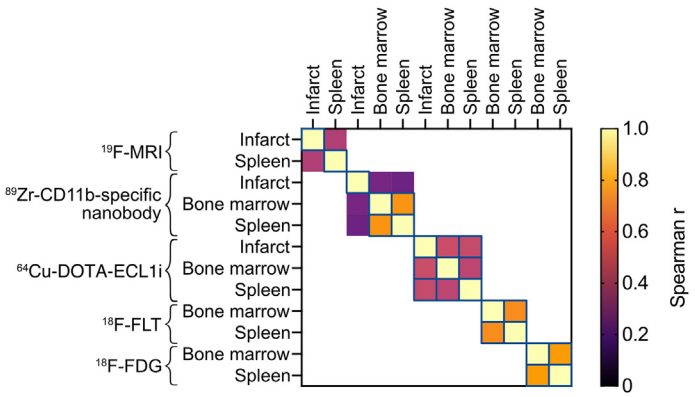

Heatmap showing correlations between tracer uptake in the infarct, spleen, and bone marrow. For ^{19}F-MRI, in vivo TBRs were used. For the PET tracers, ex vivo gamma counting data were used. Colors represent Spearman's *r*, and significant correlations are outlined by a **blue line**. For simplicity, inverse correlations were converted to positive values. See Supplemental Figure 6 for individual graphs.

in the spleens in both myocardial infarction models, compared with naïve controls ($P = 0.039$ control vs IR; $P = 0.039$ control vs PO) (Supplemental Figures 5l to 5n). Taken together, these data show that there is little difference in splenic activity between the two myocardial infarction models, as assessed by multimodal imaging.

CORRELATION BETWEEN TRACER UPTAKE IN THE HEMATOPOIETIC ORGANS AND THE INFARCTED MYOCARDIUM. We subsequently evaluated the correlations between tracer uptake in the infarct, spleen, and bone marrow (**Figure 4,** Supplemental Figure 6). For ^{89}Zr-CD11b-specific nanobody, ^{18}F-FLT, and ^{18}F-FDG, we found significant correlations between tracer uptake in the bone marrow and spleen. This correlation was weaker for ^{64}Cu-DOTA-ECL1i. However, we detected a significant correlation between ^{64}Cu-DOTA-ECL1i accumulation in the hematopoietic organs and the infarct. These findings highlight the importance of evaluating multiple tissues simultaneously.

ATHEROSCLEROSIS ACCELERATES IN BOTH TYPES OF MYOCARDIAL INFARCTION. Systemic inflammation after IR and PO was mainly caused by myocardial ischemia; we did not detect higher numbers of circulating inflammatory immune cells after sham surgery (Supplemental Figure 4c). Seven days after infarction, circulating neutrophils were still elevated, with no differences between the models (Supplemental Figure 7), indicating ongoing inflammatory activity and leukocyte supply from the hematopoietic organs. We therefore tested the long-term impact of these two types of cardiac ischemia on atherosclerosis. We know that PO results in accelerated atherosclerosis,[5] but whether IR has the same impact is unknown. To explore this, we exposed atherosclerosis-prone *Apoe*$^{-/-}$ mice to a Western diet for 6 weeks before inducing IR or PO. We performed cardiac MRI 2 days after ischemia to assess infarct size and cardiac function. Four weeks later, we investigated the effects on plaque and systemic inflammation (**Figure 5A**). We found larger infarcts and greater reduction in LVEF in *Apoe*$^{-/-}$ PO mice compared with *Apoe*$^{-/-}$ IR mice ($P < 0.001$) (**Figures 5C to 5D**). In addition, atherosclerotic mice subjected to PO had worse survival than their littermates subjected to IR (**Figure 5E**). These patterns are similar to our findings in wild-type mice (**Figures 1F to 1I**).

Flow cytometric analyses 4 weeks after infarction disclosed more Ly6C^{hi} monocytes in the femurs of mice subjected to PO as compared to controls ($P = 0.035$), while splenic Ly6C^{hi} monocyte numbers increased in both cardiac ischemia models ($P < 0.001$ control vs IR; $P = 0.003$ control vs PO) (**Figure 5F**). In addition, we found elevated numbers of CD11b^{+} myeloid cells in the spleens of IR and PO mice ($P = 0.063$ control vs IR; $P = 0.071$ control vs PO) (Supplemental Figure 8a). We subsequently assessed the impact of the different myocardial ischemia types on plaque size and myeloid cell content. Flow cytometry analysis performed 4 weeks after infarction showed significantly higher CD11b^{+} cell numbers in the aortas of IR and PO mouse models, compared with atherosclerotic mice that were not subjected to myocardial infarction ($P < 0.001$ control vs IR; $P = 0.018$ control vs PO) (Supplemental Figure 8b). This higher count was mainly due to raised macrophage numbers ($P < 0.001$ control vs IR; $P = 0.030$ control vs PO). In addition, we found expanded Ly6C^{high} monocyte numbers in the aortic plaque in both myocardial ischemia models compared with control mice ($P = 0.002$ control vs IR; $P = 0.021$ control vs PO) (**Figure 5G**). We observed a larger mac3^{+} area in the aortic root of PO mice compared with mice without infarction ($P = 0.093$ control vs IR; $P = 0.011$ control vs PO) (**Figures 5H and 5I**). Also, aortic root lesions were significantly larger in mice subjected to PO and trended toward larger in IR mice ($P = 0.079$ control vs IR; $P = 0.010$ control vs PO). Furthermore, we found an inverse correlation between plaque size and cardiac function (**Figure 5J**).

FIGURE 5 Ischemia-Reperfusion and Permanent Occlusion Similarly Accelerate Atherosclerosis

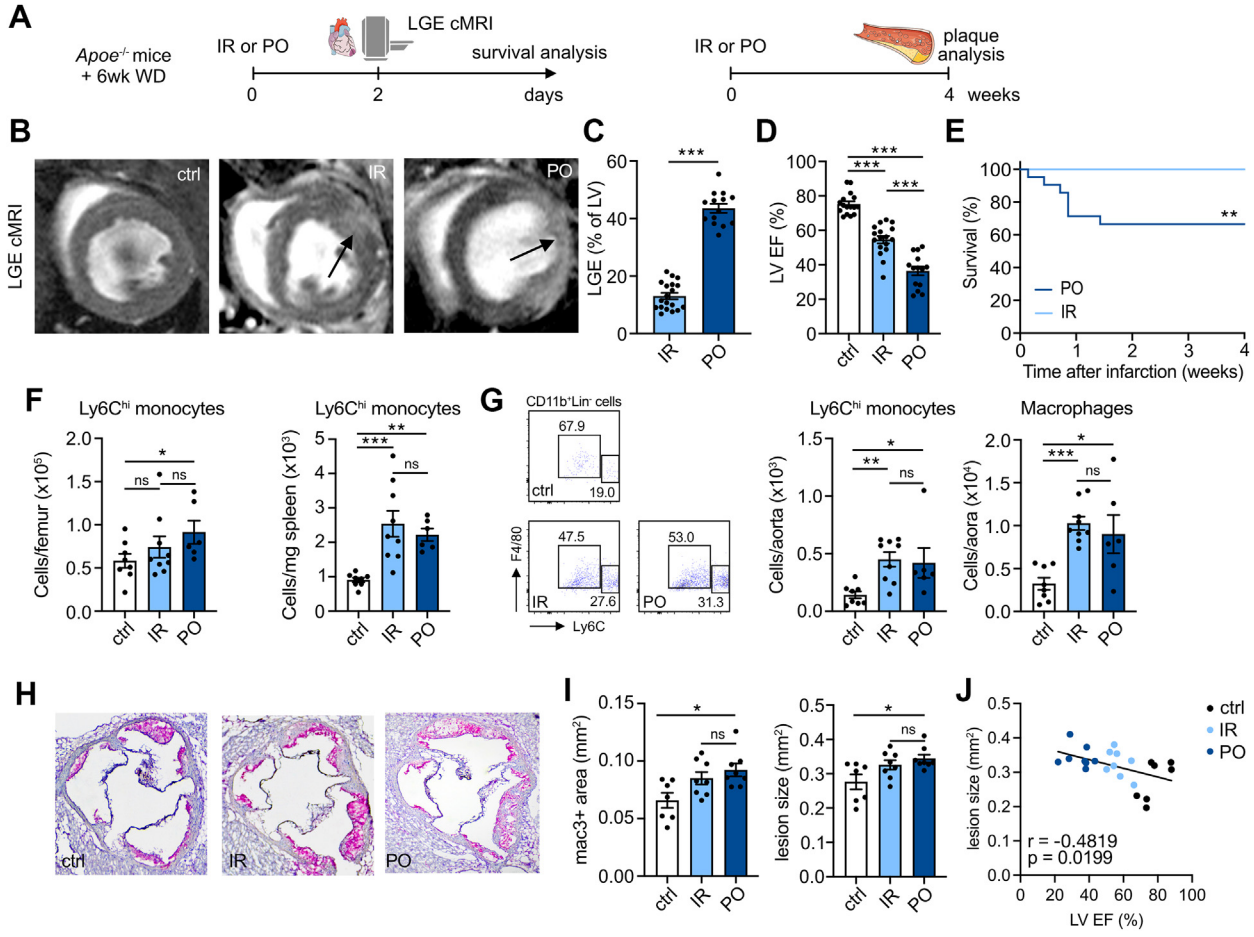

(A) Eight-week-old *Apoe*$^{-/-}$ mice were fed a Western diet (WD) for 6 weeks before IR or PO surgery. Two days after cardiac ischemia, LGE cardiac MRI was performed. Mice were followed for survival. Plaque analyses were performed 4 weeks after IR/PO surgery. **(B)** Representative LGE cMR images; **arrows** indicate infarct area. **(C)** LGE area in % of the left ventricle (n = 14-19; ***P <0.001; 2-tailed Student's t-test). **(D)** LVEF of control, IR, and PO *Apoe*$^{-/-}$ mice (n = 14–17; $P < 0.001$ for IR vs PO, control vs IR, and control vs PO; 1-way ANOVA). **(E)** *Apoe*$^{-/-}$ mice with IR injury had better survival than those with PO surgery (n = 23-25; log-rank test: $P = 0.006$). **(F)** Ly6C^{high} monocyte numbers in the bone marrow (n = 6-9; $P = 0.50$ control vs IR; $P = 0.035$ control vs PO; $P = 0.12$ IR vs PO; Kruskal-Wallis test) and spleen (n = 6-9; $P < 0.001$ control vs IR; $P = 0.003$ control vs PO; $P = 0.90$ IR vs PO; Kruskal-Wallis test) of *Apoe*$^{-/-}$ mice 4 weeks after IR/PO surgery. **(G)** Ly6C^{high} monocyte (n = 6-9; $P = 0.002$ control vs IR; $P = 0.021$ control vs PO; $P = 0.66$ IR vs PO; Kruskal-Wallis test) and macrophage (n = 6-9; $P < 0.001$ control vs IR; $P = 0.030$ control vs PO; $P = 0.31$ IR vs PO; Kruskal-Wallis test) numbers in aortas of *Apoe*$^{-/-}$ mice 4 weeks after IR/PO surgery, with representative flow cytometry plots. **(H)** Representative images of mac3/hematoxylin–stained aortic roots 4 weeks after IR/PO surgery. **(I)** Mac3^{+} area (n = 6-9; $P = 0.093$ control vs IR; $P = 0.011$ control vs PO; $P = 0.38$ IR vs PO; Kruskal-Wallis test) and lesion size (n = 6-9; $P = 0.079$ control vs IR; $P = 0.010$ control vs PO; $P = 0.40$ IR vs PO; Kruskal-Wallis test) were both significantly larger in PO mice compared with control mice. IR mice had a trend toward larger macrophage area and lesion size in aortic roots. **(J)** Correlation between LVEF and lesion size. Data are presented as mean ± SEM, unless otherwise specified. *P <0.05; **P <0.01; ***P <0.001. Abbreviations as in Figures 1 and 2.

These data show that: 1) IR and PO myocardial infarction induce distinct cardiac phenotypes in mice with atherosclerosis, similar to outcomes seen in wild-type mice; 2) myocardial infarction accelerates atherosclerosis, as previously shown;[5] and 3) this happens regardless of which model of myocardial infarction is used.

DISCUSSION

In this study, we characterized the inflammatory response after myocardial infarction in permanent and temporary LAD occlusion models by means of multiple PET and MRI approaches to probe myeloid cell dynamics and hematopoietic activity. Our data

show that these two murine models of myocardial infarction induce similar systemic inflammation profiles and exacerbate atherosclerosis. At the same time, the models have notably different effects on cardiac function, with more favorable outcomes in the reperfusion model.

As our findings show, the reperfusion model generates smaller infarcts, accompanied by better cardiac function and improved survival rates, compared with the permanent coronary artery occlusion model. These data align with results from previous studies.[18,19] Recent work by Pluijmert et al[17] observed reduced inflammatory leukocyte influx into the infarct zone of mice with temporal coronary artery occlusion compared with permanent occlusion. We expand on this research by revealing systemic immune activation patterns in the hematopoietic organs (ie, spleen and bone marrow) after both temporal and permanent coronary artery occlusion. Moreover, we found that both models accelerate atherosclerotic plaque inflammation via enhanced systemic supply of leukocytes.

A pressing need exists for clinical readouts of inflammatory activity in cardiovascular disease. Therefore, developing and applying systemic noninvasive imaging techniques is critical. The present study deployed molecular imaging protocols with innovative radiotracers to assess immune cell dynamics locally—in the infarcted myocardium—as well as systemically—in the bone marrow and spleen. In addition to ^{18}F-FDG PET, ^{18}F-FLT PET, ^{64}Cu-DOTA-ECL1i PET, and LGE-MRI, which are currently being used in the clinic or evaluated in clinical trials, we used CD11b-specific nanobody PET and nanotracer-based ^{19}F-MRI, which are now preclinical research methods.[22,23,27]

In the context of cardiovascular disease, ^{18}F-FDG PET imaging is increasingly applied to gauge (chronic) inflammatory activity in spleen, bone marrow, and atherosclerotic plaque. Recent studies showed that patients with atherosclerotic cardiovascular disease have enhanced ^{18}F-FDG uptake in spleen and bone marrow, corresponding with higher hematopoietic activity levels.[34] Moreover, ^{18}F-FDG uptake in the spleen independently predicts risk of subsequent cardiovascular events.[35] Elevated ^{18}F-FDG uptake in the bone marrow was even found to be an early indicator of atherosclerosis.[36] Our study successfully used this imaging method to detect the acute inflammatory response after myocardial infarction. We obtained similar findings through ^{18}F-FLT PET imaging, which could therefore serve as an alternate approach.[37]

The CD11b PET imaging method is based on an ^{89}Zr-labeled CD11b-binding nanobody, which, unlike ^{18}F-FDG and ^{18}F-FLT PET, is cell type specific. Nanobodies are the smallest antigen-binding derivative obtainable from naturally occurring antibodies.[25] Several nanobody-based tracers have been developed for other targets and are presently being evaluated in preclinical and clinical settings.[38] In the present study, we effectively used CD11b-specific nanobodies to capture myeloid cell influx into the ischemic myocardium. We also detected a reduction tracer signal in bone marrow after myocardial infarction. Although there is enhanced myelopoiesis at this stage, we think that the drop in PET signal is caused by ^{89}Zr-labeled CD11b^{+} cell egress from the bone marrow during the 24 hours between tracer administration and imaging. Detecting this phenomenon could be informative for preclinical studies. However, for clinical applications, labeling with a shorter-lived isotope (eg, ^{18}F) would be preferable. This would shorten the interval between tracer administration and imaging, thereby reducing the opportunity to capture myeloid cell egress.

The PET tracer ^{64}Cu-DOTA-ECL1i targets CCR2-expressing inflammatory monocytes and macrophages. The tracer effectively detects inflammation in mouse models of aortic aneurysm and myocardial infarction.[16,30] It also binds inflammatory lesions in human tissue specimens taken from patients with myocardial infarction and chronic ischemic heart disease.[15] Moreover, this tracer has had promising results in patients with lung fibrosis[29,31] and is currently being tested in patients with myocardial infarction (NCT05107596). Here, we successfully used this radiotracer to visualize CCR2^{+} cell recruitment to the infarcted myocardium in both infarction models; however, CCR2 PET was less informative for systemic inflammation. Although this imaging method and CD11b PET imaging similarly detect immune cell influx into the myocardium, the two approaches differ. On one hand, ^{64}Cu-DOTA-ECL1i does not bind to, for example, CCR2^{-} resident macrophages, resulting in more specific detection of inflammatory activity. On the other hand, CD11b PET might be the preferred method for including neutrophils, which are important players in the immediate response to myocardial infarction.[26,29]

We have previously demonstrated the value of ^{19}F-MRI in assessing cardiac inflammation and myeloid cell migration from the spleen.[22] Here, we applied PERFECTA nanomaterials to investigate the immune response after myocardial infarction in two different mouse models. Perfluorocarbons (PFCs) are considered biologically inert, providing favorable characteristics for clinical applications. For example, they are already used as oxygen carriers in blood

substitutes.[39] Nienhaus et al[40] demonstrated that human monocyte function and viability were maintained after PFC uptake. In line with our previous work,[22] we observed decreased ^{19}F-MRI signal in the spleen after permanent LAD ligation. However, we did not see this phenomenon in the IR mouse model: In those animals, ^{19}F-MRI signal in the spleen was similar to that in naïve mice. This difference could not be attributed to distinct patterns of myeloid cell migration from the spleen to the circulation, because we detected similar levels of CD11b^{+} cells in the peripheral blood of both myocardial infarction groups. Furthermore, ^{89}Zr-CD11b-specific nanobody and ^{64}Cu-DOTA-ECL1i accumulated similarly in the spleen in both models. Further research is needed to explain the varied ^{19}F-MRI signal in the spleen. Potentially, PERFECTA nanotracer behavior could be more susceptible to cardiac function differences between the models, given its larger size and longer circulation time compared with the two radiotracers.

CONCLUSIONS

In summary, we developed and used multimodal, multiparametric imaging protocols to characterize the immune response in the heart, bone marrow, and spleen in 2 models of myocardial infarction. These efforts contribute to the urgently needed development of clinical readouts of inflammatory activity in cardiovascular disease, to be used as both prognostic markers of disease outcomes and criteria for characterizing the efficacy of new immunomodulating drugs.

ACKNOWLEDGMENTS The authors thank the Flow Cytometry Core and the BMEII Small Animal Imaging Facility at the Icahn School of Medicine at Mount Sinai. They thank Omar Abousaway for technical assistance. They acknowledge Servier Medical Art for cartoon components. They thank K. Joyes for editing the manuscript.

FUNDING SUPPORT AND AUTHOR DISCLOSURES

This work was supported by National Institute of Health grants R01HL143814 (to Dr Fayad), P01HL131478 (Drs Fayad and Mulder), P41EB025815 (Drs Liu and Gropler), R35HL145212 (Dr Liu), and R35HL139598 (Dr Nahrendorf) and award K22CA226040 (Dr Rashidian). This work was also supported by an Innovation Research Fund Basic Research Award from the Dana-Farber Cancer Institute (Dr Rashidian). Dr Maier was supported by Deutsche Forschungsgemeinschaft grants (MA 7059/1 and MA 7059/3-1) and is part of SFB1425 funded by the Deutsche Forschungsgemeinschaft (project no. 422681845). All other authors have reported that they have no relationships relevant to the contents of this paper to disclose.

ADDRESS FOR CORRESPONDENCE: Dr Mandy M.T. van Leent, Biomedical Engineering and Imaging Institute, Diagnostic, Molecular, and Interventional Radiology, Icahn School of Medicine at Mount Sinai, New York, New York 10029, USA. E-mail: mandy.vanleent@mountsinai.org.

PERSPECTIVES

COMPETENCY IN MEDICAL KNOWLEDGE: Research on atherosclerotic cardiovascular disease has uncovered inflammation to be a key driver of the pathophysiologic process. A pressing need therefore exists to quantitatively and longitudinally probe inflammation in preclinical models and in cardiovascular disease patients, ideally using noninvasive methods. In this study, we showed the strengths and capabilities of multiparametric imaging in detecting inflammatory activity in cardiovascular disease, augmenting the development of clinical readouts.

TRANSLATIONAL OUTLOOK: We show that preclinical immunoimaging can be used to comprehensively profile the immune responses following myocardial infarction. These efforts aid in the development of clinical readouts of inflammatory activity in cardiovascular disease, to be used either as prognostic markers of disease outcomes or to characterize the efficacy of novel immune modulating therapies.

REFERENCES

1. Swirski FK, Nahrendorf M, Etzrodt M, et al. Identification of splenic reservoir monocytes and their deployment to inflammatory sites. *Science*. 2009;325:612–616.

2. van der Laan AM, Ter Horst EN, Delewi R, et al. Monocyte subset accumulation in the human heart following acute myocardial infarction and the role of the spleen as monocyte reservoir. *Eur Heart J*. 2014;35:376–385.

3. Swirski FK, Nahrendorf M. Leukocyte behavior in atherosclerosis, myocardial infarction, and heart failure. *Science*. 2013;339:161–166.

4. Panizzi P, Swirski FK, Figueiredo JL, et al. Impaired infarct healing in atherosclerotic mice with Ly-6C^{hi} monocytosis. *J Am Coll Cardiol*. 2010;55:1629–1638.

5. Dutta P, Courties G, Wei Y, et al. Myocardial infarction accelerates atherosclerosis. *Nature*. 2012;487:325–329.

6. Lavine KJ, Pinto AR, Epelman S, et al. The macrophage in cardiac homeostasis and disease: JACC macrophage in CVD series (part 4). *J Am Coll Cardiol*. 2018;72:2213–2230.

7. Yellon DM, Hausenloy DJ. Myocardial reperfusion injury. *N Engl J Med*. 2007;357:1121–1135.

8. Fayad ZA, Swirski FK, Calcagno C, Robbins CS, Mulder W, Kovacic JC. Monocyte and macrophage dynamics in the cardiovascular system: JACC macrophage in CVD series (part 3). *J Am Coll Cardiol*. 2018;72:2198–2212.

9. Nahrendorf M, Frantz S, Swirski FK, et al. Imaging systemic inflammatory networks in ischemic heart disease. *J Am Coll Cardiol*. 2015;65:1583–1591.

10. von Elverfeldt D, Maier A, Duerschmied D, et al. Dual-contrast molecular imaging allows noninvasive characterization of myocardial ischemia/reperfusion injury after coronary vessel occlusion in mice by magnetic resonance imaging. *Circulation*. 2014;130:676–687.

11. Tirotta I, Mastropietro A, Cordiglieri C, et al. A superfluorinated molecular probe for highly sensitive in vivo ^{19}F-MRI. *J Am Chem Soc*. 2014;136:8524–8527.

12. Kossatz S, Carney B, Schweitzer M, et al. Biomarker based PET imaging of diffuse intrinsic pontine glioma in mouse models. *Cancer Res*. 2017;77:2112–2123.

13. Priem B, van Leent MMT, Teunissen AJP, et al. Trained immunity-promoting nanobiologic therapy suppresses tumor growth and potentiates checkpoint inhibition. *Cell*. 2020;183:786–801.e19.

14. Liu Y, Li W, Luehmann HP, et al. Noninvasive imaging of CCR2^{+} cells in ischemia-reperfusion injury after lung transplantation. *Am J Transplant*. 2016;16:3016–3023.

15. Heo GS, Kopecky B, Sultan D, et al. Molecular imaging visualizes recruitment of inflammatory monocytes and macrophages to the injured heart. *Circ Res*. 2019;124:881–890.

16. Heo GS, Bajpai G, Li W, et al. Targeted PET imaging of chemokine receptor 2–positive monocytes and macrophages in the injured heart. *J Nucl Med*. 2021;62:111–114.

17. Pluijmert NJ, Bart CI, Bax WH, Quax PHA, Atsma DE. Effects on cardiac function, remodeling and inflammation following myocardial ischemia-reperfusion injury or unreperfused myocardial infarction in hypercholesterolemic APOE*3-Leiden mice. *Sci Rep*. 2020;10:16601.

18. Michael LH, Ballantyne CM, Zachariah JP, et al. Myocardial infarction and remodeling in mice: effect of reperfusion. *Am J Physiol*. 1999;277:H660–H668.

19. de Celle T, Cleutjens JP, Blankesteijn WM, Debets JJ, Smits JF, Janssen BJ. Long-term structural and functional consequences of cardiac ischaemia-reperfusion injury in vivo in mice. *Exp Physiol*. 2004;89:605–615.

20. Mulder WJM, van Leent MMT, Lameijer M, Fisher EA, Fayad ZA, Pérez-Medina C. High-density lipoprotein nanobiologics for precision medicine. *Acc Chem Res*. 2018;51:127–137.

21. Flögel U, Ding Z, Hardung H, et al. In vivo monitoring of inflammation after cardiac and cerebral ischemia by fluorine magnetic resonance imaging. *Circulation*. 2008;118:140–148.

22. Senders ML, Meerwaldt AE, van Leent MMT, et al. Probing myeloid cell dynamics in ischaemic heart disease by nanotracer hot-spot imaging. *Nat Nanotechnol*. 2020;1:398–405.

23. Schoormans J, Calcagno C, Daal MRR, et al. An iterative sparse deconvolution method for simultaneous multicolor ^{19}F-MRI of multiple contrast agents. *Magn Reson Med*. 2020;83:228–239.

24. Rashidian M, Ingram JR, Dougan M, et al. Predicting the response to CTLA-4 blockade by longitudinal noninvasive monitoring of CD8 T cells. *J Exp Med*. 2017;214:2243–2255.

25. Teunissen AJP, Abousaway OB, Munitz J, et al. Employing nanobodies for immune landscape profiling by PET imaging in mice. *STAR Protoc*. 2021;2:100434.

26. Rashidian M, Keliher EJ, Bilate AM, et al. Noninvasive imaging of immune responses. *Proc Natl Acad Sci U S A*. 2015;112:6146–6151.

27. Rashidian M, LaFleur MW, Verschoor VL, et al. Immuno-PET identifies the myeloid compartment as a key contributor to the outcome of the antitumor response under PD-1 blockade. *Proc Natl Acad Sci U S A*. 2019;116:16971–16980.

28. Tsou C-L, Peters W, Si Y, et al. Critical roles for CCR2 and MCP-3 in monocyte mobilization from bone marrow and recruitment to inflammatory sites. *J Clin Invest*. 2007;117:902–909.

29. Liu Y, Gunsten SP, Sultan DH, et al. PET-based imaging of chemokine receptor 2 in experimental and disease-related lung inflammation. *Radiology*. 2017;283:758–768.

30. English SJ, Sastriques SE, Detering L, et al. CCR2 positron emission tomography for the assessment of abdominal aortic aneurysm inflammation and rupture prediction. *Circ Cardiovasc Imaging*. 2020;13:e009889.

31. Brody SL, Gunsten SP, Luehmann HP, et al. Chemokine receptor 2–targeted molecular imaging in pulmonary fibrosis. a clinical trial. *Am J Respir Crit Care Med*. 2021;203:78–89.

32. Dutta P, Sager HB, Stengel KR, et al. Myocardial infarction activates CCR2^{+} hematopoietic stem and progenitor cells. *Cell Stem Cell*. 2015;16:477–487.

33. Leuschner F, Rauch PJ, Ueno T, et al. Rapid monocyte kinetics in acute myocardial infarction are sustained by extramedullary monocytopoiesis. *J Exp Med*. 2012;209:123–137.

34. van der Valk FM, Kuijk C, Verweij SL, et al. Increased haematopoietic activity in patients with atherosclerosis. *Eur Heart J*. 2017;38:425–432.

35. Emami H, Singh P, MacNabb M, et al. Splenic metabolic activity predicts risk of future cardiovascular events: demonstration of a cardiosplenic axis in humans. *J Am Coll Cardiol Img*. 2015;8:121–130.

36. Devesa A, obo-González M, Martínez-Milla J, et al. Bone marrow activation in response to metabolic syndrome and early atherosclerosis. *Eur Heart J*. 2022;43:1809–1828.

37. Ye Y-X, Calcagno C, Binderup T, et al. Imaging macrophage and hematopoietic progenitor proliferation in atherosclerosis. *Circ Res*. 2015;117:835–845.

38. Berland L, Kim L, Abousaway O, et al. Nanobodies for medical imaging: about ready for prime time? *Biomolecules*. 2021;11:637.

39. Spahn DR. Blood substitutes. Artificial oxygen carriers: perfluorocarbon emulsions. *Crit Care*. 1999;3:R93–R97.

40. Nienhaus F, Colley D, Jahn A, et al. Phagocytosis of a PFOB-nanoemulsion for ^{19}F magnetic resonance imaging: first results in monocytes of patients with stable coronary artery disease and ST-elevation myocardial infarction. *Molecules*. 2019;24:2058.

KEY WORDS atherosclerosis, imaging, immunology, inflammation, MI

APPENDIX For supplemental figures, please see the online version of this paper.